Earth and Planetary Science Letters xxx (2008) xxx-xxx

Contents lists available at ScienceDirect

Earth and Planetary Science Letters

journal homepage: www.elsevier.com/locate/epsl

Magmatic volatile contents and degassing-induced crystallization at Volcán Jorullo, Mexico: Implications for melt evolution and the plumbing systems of monogenetic volcanoes

Emily R. Johnson [a,*], Paul J. Wallace [a], Katharine V. Cashman [a], Hugo Delgado Granados [b], Adam Kent [c]

[a] Department of Geological Sciences, University of Oregon, Eugene, OR 97405-1272 USA
[b] Departamento de Vulcanología, Instituto de Geofísica, UNAM Ciudad Universitaria 04510 México, D.F., Mexico
[c] Department of Geosciences, 104 Wilkinson Hall, Oregon State University, Corvallis, Oregon, 97330 USA

ARTICLE INFO

Article history:
Received 14 September 2007
Received in revised form 27 February 2008
Accepted 1 March 2008
Available online xxxx

Editor: R.W. Carlson

Keywords:
melt inclusions
volatiles
degassing
crystallization
basalt
cinder cone

ABSTRACT

Monogenetic basaltic cinder cones are abundant on Earth and exhibit a wide range of eruptive styles, including violent explosions. However, the mechanisms driving explosive cinder cone eruptions are still poorly understood. Here we investigate relations between volatiles, degassing, and crystallization in a long-lived, historical, cinder cone eruption to better understand the plumbing systems of monogenetic volcanoes. We present volatile (H_2O, CO_2, S, Cl), major, and trace element data for olivine-hosted melt inclusions, estimates of olivine residence times based on Fe–Mg zoning, and measurements of groundmass crystallinity for tephra from the eruption of Volcán Jorullo, Mexico. Jorullo melt inclusions trapped some of the most volatile-rich (≤5.3 wt.% H_2O, ≤1000 ppm CO_2), primitive (≤10.5 wt.% MgO) melts yet measured in an arc setting, as well as more degassed, evolved compositions. Furthermore, the melt inclusions record temporal changes in both melt composition and crystallization. Early erupted inclusions are Mg-rich and record variable trapping pressures (10–400 MPa), whereas late inclusions were trapped only shallowly beneath the volcano (3–19 MPa) and contain increasingly evolved melts. Disparities between the compositions of the melt inclusions and the whole-rock lava samples provide evidence for a two-stage crystallization process: 1) cooling-induced fractionation of amphibole+olivine±clinopyroxene in the lower crust, which drove the bulk melt evolution over time; and 2) degassing-induced crystallization of melts during ascent at pressures <400 MPa. Additionally, olivine residence times calculated from diffusion profiles suggest that as the eruption progressed, olivine crystals were being stored for longer periods of time (up to 1300 days) within more evolved melts that had risen from depth. These data, taken together with temporal decreases in crystallization depths and increases in groundmass crystallinity, suggest the formation of a shallow reservoir (or simply an enlarged region of the conduit) beneath the volcano late in the eruption. Shallow storage permitted degassing and crystallization of the Jorullo melts, and facilitated assimilation of the host rock by the resident magma.

© 2008 Published by Elsevier B.V.

1. Introduction

Water is fundamental to magma production in subduction zones by initiating melting of the mantle wedge above the downgoing slab. Furthermore, the presence of water and other volatiles in magma prior to eruption affects crystallization during ascent and eruption explosivity. Melt inclusion analyses have shown that arc magmas can have high H_2O (3.5–8 wt.%; Sisson and Layne, 1993; Roggensack et al., 1997; Cervantes and Wallace, 2003; Wade et al., 2006; Spilliaert et al., 2006) that may correlate with high explosivity (Roggensack et al., 1997; Spilliaert et al., 2006). Degassing of these H_2O-rich magmas during ascent may also induce rapid and extensive crystallization (e.g., Sisson and Layne, 1993; Métrich et al., 2001; Roggensack, 2001; Atlas et al., 2006; Blundy et al., 2006). However, most studies have focused on persistently active, larger volcanoes, often with evolved melt compositions.

Our research focuses on high-Mg basaltic magmas from a cinder cone eruption. Cinder cones are the most numerous volcanoes on land (Vespermann and Schmincke, 2002), and due to their small volumes and relatively short eruption durations (~1 day to 15 yr), the magmas often undergo limited evolution by fractional crystallization and assimilation. In spite of their relative abundance, the hazards posed by cinder cone eruptions are commonly underestimated, and the eruption processes that form cinder cones are not well understood. Most cinder cone eruptions are brief (<1 yr; Wood, 1980) and the magmas do not evolve over the course of the eruption. Longer lived eruptions, like Jorullo and Parícutin in Mexico (15 and 9 yr,

* Corresponding author. Tel.: +1 541 337 0693; fax: +1 541 346 4692.
E-mail address: ejohns10@uoregon.edu (E.R. Johnson).

0012-821X/$ – see front matter © 2008 Published by Elsevier B.V.
doi:10.1016/j.epsl.2008.03.004

UNCORRECTED PROOF

ARTICLE IN PRESS

respectively) are more complex; at both volcanoes, magmas evolved progressively during the eruptions, and such evolution has been explained by combinations of fractional crystallization and crustal assimilation (McBirney et al., 1987; Luhr, 2001; Rubin et al., 2004). Recently, fractionation and assimilation in the lower crust in a "deep crustal hot zone" (Annen et al., 2006) or "MASH zone" (Hildreth and Moorbath, 1988) has been invoked to explain intermediate magma compositions erupted from long-lived stratovolcanoes. However, in monogenetic systems, where do fractionation and assimilation occur? A recent study of an eroded cinder cone has shown a network of dikes and sills feeding the volcano just beneath the surface (Valentine and Krogh, 2006). Such a network provides possible shallow magma storage locations where magma could evolve in composition; however, the development and evolution of such plumbing systems during the course of an eruption are not known.

Here we use melt inclusions trapped in forsterite (Fo)-rich olivine (Fo_{85-91}, where Fo = 100 * Mg/(Mg + Fe)), combined with measurements of melt crystallinity and estimates of crystal residence times and magma storage depths, to characterize changes in the plumbing system during the eruption of Jorullo. Our data constrain the undegassed, near-primary volatile contents of the melt and track the degassing, crystallization and compositional evolution of the magma before and during the eruption, thereby providing new insight into cinder cone eruption processes. Our results show that cinder cones, in spite of their relatively small size, are capable of evolving both compositionally and structurally during eruption. In longer-lived eruptions like Jorullo (15 yr), the plumbing systems may be more complex than a simple feeder-dike.

2. Geologic setting and eruption history

Jorullo is located in the Michoacán–Guanajuato Volcanic Field (MGVF), in the central part of the subduction-related Trans-Mexican Volcanic Belt (Fig. 1). Volcanism in the MGVF is due to subduction of the Cocos plate beneath the North American plate off the southwest coast of Mexico. The MGVF contains nearly 1000 cinder cones, many of them Holocene in age (Hasenaka and Carmichael, 1985). Jorullo is located along the volcanic front in the MGVF, roughly 80–90 km above the Cocos plate (Pardo and Suárez, 1995). The most recent activity in the MGVF was the eruption of the cinder cone Parícutin from 1943–1952, 84 km NW of Jorullo.

Jorullo erupted from 1759 until 1774, producing a thick blanket of tephra and ash as well as numerous lava flows (Luhr and Carmichael, 1985). Early accounts indicate that the eruption began violently, with explosive activity that persisted for many years (Gadow, 1930). These accounts, combined with the abundance of fine ash in the tephra blanket, suggest that like Parícutin, Jorullo exhibited violent Strombolian activity, which is characterized by simultaneous explosive eruptions producing large amounts of fine ash and effusion of lava from the base of the cone (Pioli and Cashman, 2006). The widespread lava flows at Jorullo were the focus of an important study by Luhr and Carmichael (1985) that described the eruption and the compositional evolution of the lavas over time. They noted that the earliest lavas were primitive basalt, with 9.3 wt.% MgO and phenocrysts of magnesian olivine (Fo_{86-90}), and that as the eruption progressed, the lavas evolved to basaltic andesite compositions (Luhr and Carmichael, 1985).

3. Sample description and analytical procedures

We present results from two sections excavated through the tephra deposit, located ~1 km from the vent to the south and southeast, respectively (Fig. 1). The tephra sections expose the earliest erupted explosive material (in contact with the underlying paleosol) and are composed of bedded ash and lapilli layers that provide a time sequence of the eruption. The tephra also contains abundant, loose

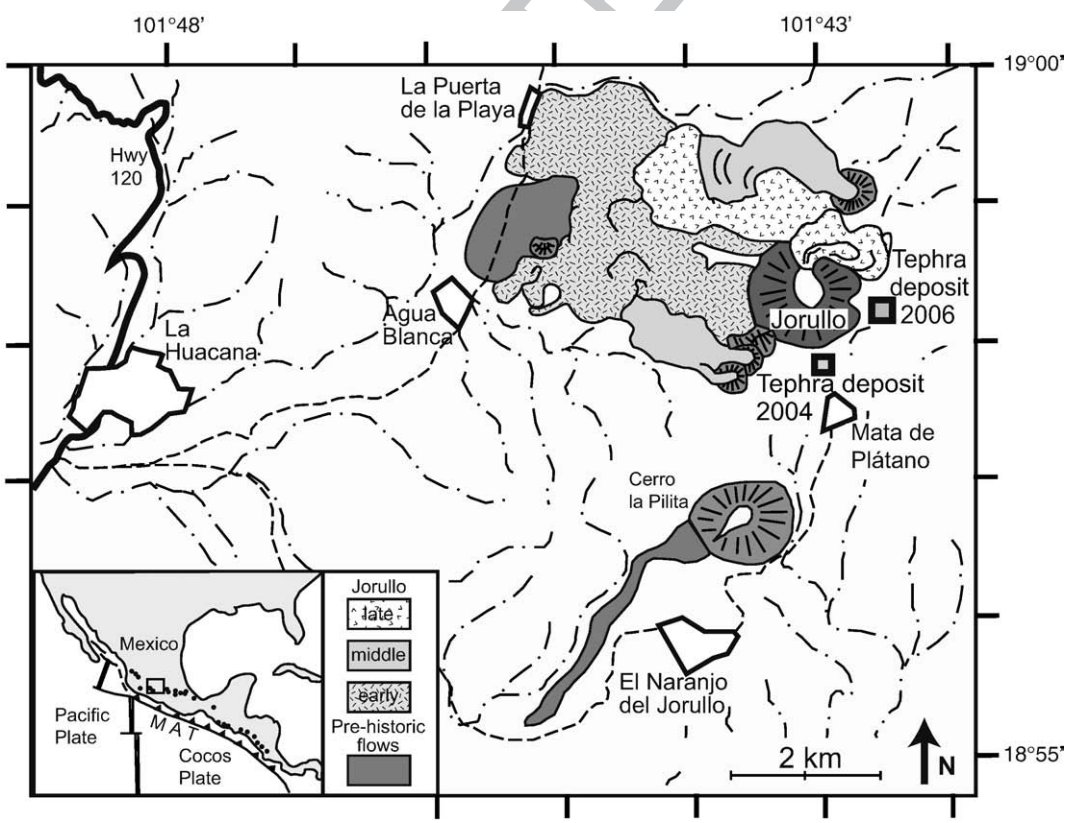

Fig. 1. Map of Jorullo and surrounding area, modified from Luhr and Carmichael (1985). Squares mark locations of the two tephra sections used in this study; the 2004 section contains the 'Early' (in contact with the paleosol) and 'Middle' samples, and the more complete 2006 section contains the 'Late' sample. Inset shows plate tectonic boundaries associated with the Trans-Mexican Volcanic Belt, with major volcanoes shown as dots.

Please cite this article as: Johnson, E.R., et al., Magmatic volatile contents and degassing-induced crystallization at Volcán Jorullo, Mexico: Implications for melt evolution and the plumbing systems..., Earth Planet. Sci. Lett. (2008), doi:10.1016/j.epsl.2008.03.004

olivine phenocrysts throughout the section. Samples for this study were chosen from three representative tephra layers – the basal (in contact with the paleosol), middle, and upper parts of the section – that will be referred to as the 'early', 'middle', and 'late' samples, respectively.

We analyzed olivine-hosted melt inclusions to obtain pre-eruptive volatile and melt compositions. Loose olivine crystals from each of the three layers were separated, cleaned in HBF_4, and examined in immersion oil (refractive index 1.678). Most olivine crystals are euhedral, but subhedral and skeletal crystals are also present. Melt inclusions identified as suitable (those that are fully enclosed by host crystal, are bubble-poor, and appear to be sealed) were prepared as doubly polished wafers and were analyzed for H_2O and CO_2 (FTIR), major elements, S, and Cl (electron microprobe), and trace elements (laser ablation ICP-MS). Melt inclusion compositions were corrected for post-entrapment crystallization of olivine and Fe-loss; corrected values are shown in Table 1 and uncorrected values are shown in Supplementary Table 1 (for details on the correction method and error propagation see Supplementary material). All data shown in figures and discussed in the text are corrected values. Bulk tephra samples from the three layers were analyzed by XRF at Washington State University for major and trace elements (Supplementary data Table 2). We also analyzed the compositions of olivine phenocrysts (Table 1) and tephra groundmass glass (Supplementary data Table 3) throughout the tephra stratigraphy. Major elements, S, and Cl were measured with a Cameca SX-100 electron microprobe at the University of Oregon using a 15 kV accelerating voltage, 10 nA beam current, and a beam diameter of 10 μm. A combination of glass and mineral standards was used. Trace element concentrations in the melt inclusions were measured by laser ablation ICP-MS at Oregon State University (Supplementary data Table 4). Details of the technique are found in Kent et al. (2004).

Water and CO_2 concentrations in melt inclusions were analyzed by Fourier Transform Infrared Spectroscopy (FTIR) at the University of Oregon. Concentrations of H_2O and CO_2 were calculated using Beer's law: $c = MA/\rho d\varepsilon$, where M is the molecular weight of H_2O or CO_2, A is the measured absorbance of the band of interest, ρ is the room temperature density of basaltic glass, d is the thickness of the melt inclusion and ε is the molar absorption coefficient. In most samples, water concentrations were calculated using the total OH peak at 3550 cm^{-1} and an absorption coefficient of 63 ± 3 L/mol cm (P. Dobson et al., unpublished data, cited by Dixon et al., 1995). In some instances, however, total H_2O was calculated using an average of the molecular H_2O peaks at 1630 cm^{-1} and 5200 cm^{-1} and the OH^- peak at 4500 cm^{-1}. In these cases absorption coefficients were calculated based on major element compositions (Dixon et al., 1995) and are as follows: 1630 cm^{-1} = 26.4 L/mol cm, 5200 cm^{-1} = 0.66 L/mol cm, 4500 cm^{-1} = 0.56 L/mol cm. CO_2 was calculated using the carbonate peaks at 1515 and 1435 cm^{-1}; an absorption coefficient

PROOF

Table 1
Corrected melt inclusion oxides and volatiles, host olivine compositions, and inclusion entrapment pressures

Group inclusion	Early 1	Early 12_1	Early 12_2	Early 12_3	Early 13_1	Early 13_2	Early 14	Early 17_1	Early 17_2	Early 17_A	Early 20	Early 23	Early 24	Early 28	Early 29_1	Early 29_3
SiO_2	51.15	51.54	52.06	51.58	50.60	50.11	50.93	52.90	51.32	51.19	51.22	50.63	49.89	51.57	51.01	50.26
TiO_2	0.79	0.68	0.63	0.75	0.88	0.75	0.67	0.74	0.80	0.74	0.88	0.75	0.73	0.65	0.76	0.71
Al_2O_3	15.66	16.77	17.25	16.96	18.90	19.46	17.15	16.44	17.21	17.46	16.74	17.15	17.87	16.63	17.69	17.55
FeO^T	7.84	7.38	7.30	7.36	7.65	7.26	7.46	7.47	7.52	7.41	7.55	7.56	7.62	7.48	7.65	7.57
MnO	0.15	0.13	0.06	0.08	0.08	0.21	0.02	0.10	0.10	0.04	0.15	0.07	0.05	0.10	0.14	0.09
MgO	10.51	9.23	9.00	9.44	7.75	7.43	9.99	9.29	9.64	9.25	9.91	10.03	10.46	9.82	8.69	9.56
CaO	9.20	9.34	8.57	8.91	8.92	9.21	9.01	8.28	8.55	8.93	9.14	8.96	8.60	8.55	8.92	9.21
Na_2O	3.74	4.13	4.20	4.04	4.26	4.59	3.89	4.01	4.04	4.17	3.60	4.00	3.92	4.25	4.21	4.21
K_2O	0.77	0.65	0.77	0.73	0.81	0.83	0.70	0.65	0.67	0.68	0.61	0.66	0.72	0.84	0.77	0.66
P_2O_5	0.18	0.15	0.16	0.15	0.16	0.16	0.17	0.13	0.15	0.14	0.19	0.19	0.14	0.12	0.16	0.16
H_2O	0.9	4.7	2.5	4.2	3.4	n.a.	1.2	5.4	2.6	n.a.	1.5	3.8	2.2	1.0	2.9	3.4
CO_2 ppm	118	243	207	915	–	n.a.	307	805	692	n.a.	594	988	–	–	358	556
S ppm	1149	1195	1379	1751	1591	1560	1718	1751	1665	2066	1847	1882	1776	688	1737	1644
Cl ppm	1103	1179	1197	1239	1285	1406	1381	1239	1308	1286	1267	1196	1185	1105	1176	1206
Total *	99.17	97.05	97.18	96.28	97.07	98.22	97.50	96.18	96.14	95.42	95.34	94.10	95.88	96.99	96.36	96.72
P (bars)	343	2542	1064	3445	1152	n.a.	808	4027	2080	n.a.	1481	3444	515	101	1668	2309
Olivine (Fo%)	91.1	90.3	89.9	90.4	88.4	88.4	90.5	90.1	90.3	90.1	90.5	90.7	90.6	90.0	89.3	90.2
%PEC **	14.2	6.9	12.4	10.6	3.5	4.4	17.9	9.1	12.5	9.7	11.6	10	20.6	18	8.5	11

Group inclusion	Middle 4	Middle 5	Middle 6	Middle 7_1	Middle 10	Late 1	Late 3_1	Late 3_2	Late 4	Late 5	Late p1	Late p2	Late p3a
SiO_2	52.92	52.99	50.15	50.24	51.70	51.34	52.54	55.21	53.66	51.95	50.66	54.13	55.14
TiO_2	0.76	0.88	0.90	0.89	0.76	0.98	0.95	1.12	0.88	0.84	1.06	0.98	0.91
Al_2O_3	17.42	18.09	20.14	19.69	20.32	19.83	19.07	18.02	18.01	20.42	20.25	18.59	17.87
FeO^T	7.48	6.75	6.79	7.07	6.92	6.76	7.07	6.69	7.47	6.68	6.89	6.73	6.76
MnO	0.12	0.11	0.10	0.12	0.07	0.08	0.15	0.03	0.06	0.10	0.08	0.06	0.04
MgO	7.26	6.53	5.97	6.93	6.80	6.06	5.83	5.53	5.91	5.15	6.15	6.05	6.06
CaO	9.05	8.87	10.61	9.70	7.28	9.71	8.96	8.29	8.13	9.55	9.50	8.26	8.72
Na_2O	4.02	4.45	4.32	4.30	5.06	4.29	4.34	4.07	4.66	4.24	4.50	4.28	3.72
K_2O	0.82	1.15	0.83	0.84	0.93	0.74	0.85	0.85	1.02	0.83	0.72	0.75	0.60
P_2O_5	0.15	0.17	0.20	0.21	0.17	0.22	0.23	0.20	0.20	0.24	0.19	0.17	0.17
H_2O	1.4	0.5	1.1	1.1	0.8	0.5	0.8	0.8	0.8	1.0	n.a.	n.a.	n.a.
CO_2 ppm	–	–	–	–	–	–	–	–	–	–	n.a.	n.a.	n.a.
S ppm	1407	1299	2040	1786	1781	1442	1143	74	918	1490	2106	1477	1479
Cl ppm	910	1247	1094	1127	1419	1239	1162	1020	994	1065	1298	1206	936
Total*	99.47	102.86	97.24	99.93	100.11	100.10	100.01	99.25	99.39	98.51	100.02	100.00	99.96
P (bars)	186	24	115	121	62	26	64	65	68	87	n.a.	n.a.	n.a.
Olivine (Fo%)	88.2	88.0	86.6	88.4	87.3	86.7	85.6	85.6	84.9	85.0	86.7	86.2	86.8
%PEC**	4.8	6.7	2.0	3.8	11.2	4.5	5.9	6.4	8.1	1.6	4.1	11.8	2.3

Total* = sum of all oxides plus S and Cl in original (uncorrected) microprobe analyses, %PEC** = wt.% post-entrapment crystallization. All melt inclusion data were corrected for post-entrapment crystallization (%PEC) of olivine (Sobelev and Chaussidon, 1996) and diffusive loss of Fe (Danyushevsky et al., 2000; see Supplementary material). Major element oxides reported are normalized to 100% on a volatile-free basis. The average standard deviation (absolute) based on multiple (2–4 points) analyses is as follows: SiO_2: 0.27, Al_2O_3: 0.20, FeO: 0.16, MgO: 0.22, CaO: 0.36, Na_2O: 0.27, K_2O: 0.03, TiO_2: 0.10, MnO: 0.05, P_2O_5: 0.03, S: 0.009, Cl: 0.006.

Please cite this article as: Johnson, E.R., et al., Magmatic volatile contents and degassing-induced crystallization at Volcán Jorullo, Mexico: Implications for melt evolution and the plumbing systems..., Earth Planet. Sci. Lett. (2008), doi:10.1016/j.epsl.2008.03.004

ARTICLE IN PRESS

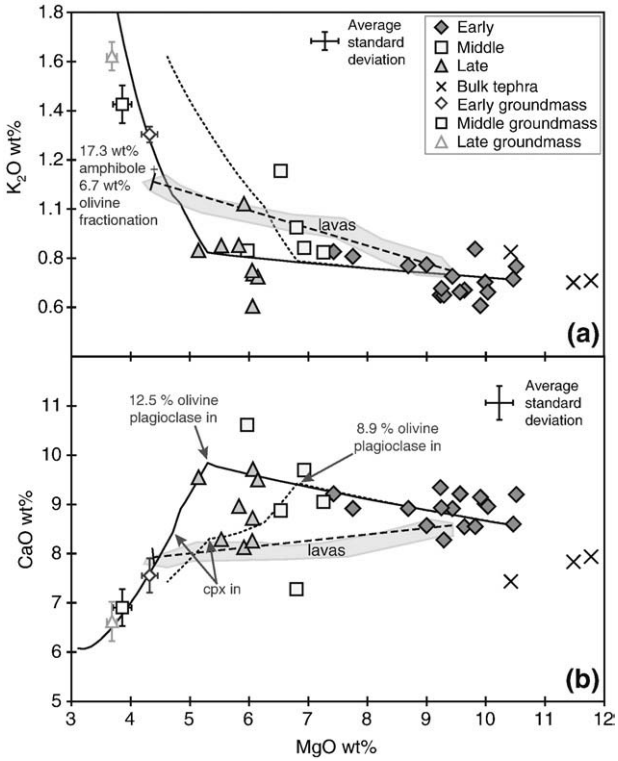

Fig. 2. Major elements vs. MgO for Jorullo melt inclusions, tephra groundmass glass, bulk tephra, and lava whole-rock samples (lava analyses are from Luhr and Carmichael, 1985). In both figures, MELTS calculations (see Fig. 8) indicate that olivine-only crystallization explains much of the range in MgO, K_2O, and CaO whereas some inclusions record plagioclase ± clinopyroxene crystallization. The MELTS calculations were done to simulate a probable ascent path (varying both pressure and temperature), the solid line shows an ascent path with greater cooling than the path of the dotted line. In contrast, the bulk melt evolution, as shown by the lava trend, corresponds to fractionation of 17.3 wt.% amphibole + 6.7 wt.% olivine (thick dashed line), based on major element modeling. Also shown are the average standard deviations based on multiple analyses per sample.

of 296 L/mol cm was calculated following Dixon and Pan (1995). Based on uncertainties in thickness measurements and absorbance values, average 1 standard deviation uncertainty in H_2O is ±0.2 wt.% and in CO_2 ±80 ppm. The background subtraction procedure that we used for the carbonate peaks is described in Roberge et al. (2005).

We measured compositional profiles across zoned olivine crystals by electron microprobe. We calculated residence times for the olivine crystals predicated on the assumption that the zoning was produced by a magma mixing event (discussed in Section 5.5), and followed the methods of Costa and Chakraborty (2004). We used the simple, 1-*D* diffusion equation:

$$C = C_1 + (C_o - C_1) * \mathrm{erf}\left[x/\left(2\sqrt{D*t}\right)\right] \quad (1)$$

where *C* is the concentration, *x* is distance, *D* is the diffusion coefficient, and *t* is time.

We calculated diffusion coefficients, *D*, for Fe–Mg exchange using the equation from Jurewicz and Watson (1988):

$$D_{\mathrm{Fe-Mg}} = 8 \times 10^{-7} * \exp(-29708/T)\mathrm{m}^2\mathrm{s}^{-1} \quad (2)$$

where *D* is diffusion parallel to the *c*-axis, and we assumed that $D_a = D_b = 6D_c$ (Dohmen et al., 2003). Using Eq. (1) we fit a modeled diffusion profile to our data, and calculated the time required to produce that profile. Our calculations were based on compositional profiles along the *a*- and *b*-axes of olivine crystals, and we used eruption temperatures calculated using the method of Sugawara (2000), which generally agree with eruption temperatures calculated using MELTS and pMELTS (Ghiorso and Sack, 1995; Asimow and Ghiorso, 1998; Ghiorso et al., 2002).

To track changes in crystallinity of the melts throughout the eruption we took images of the groundmass from the three representative tephra layers. Images were collected using an FEI Quanta scanning electron microscope (SEM) at the University of Oregon. These images were then analyzed using SCION image analysis software to calculate the groundmass crystallinity and the size (crystal area) of groundmass microlites for each sample.

4. Results

4.1. Melt inclusion and groundmass compositions

Jorullo lavas evolved from initially primitive basalt to basaltic andesite over the course of the ~15 yr eruption (Luhr and Carmichael, 1985). Our corrected melt inclusion compositions show a similar evolutionary pattern (Table 1), though there are some important compositional differences between melt inclusions and lavas. The early melt inclusions have high MgO (7.5–10.5 wt.%) and low K_2O (0.6–0.8 wt.%), suggesting that early olivine crystals trapped primitive melts that had undergone little to no differentiation from a parental magma (Fig. 2). The later-erupted melt inclusions sampled progressively more evolved melt compositions, with decreasing MgO (5–7.4 wt.%) and

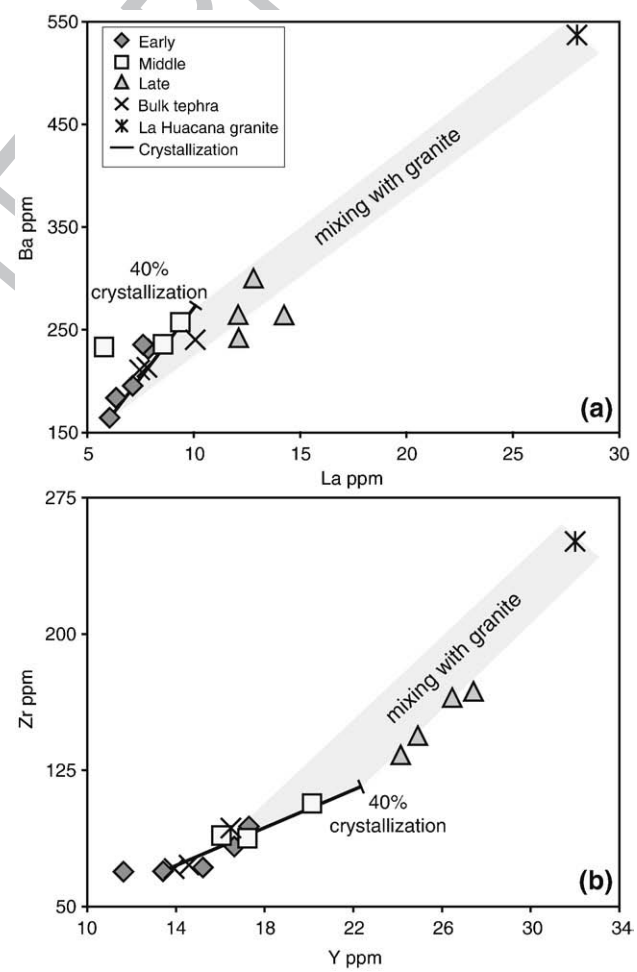

Fig. 3. Trace element analyses for melt inclusions (laser ablation ICP-MS) and bulk tephra (ICP-MS). Fig. 3a shows Ba vs. La and Fig. 3b shows Zr vs. Y. Both figures show a solid line representing 40% fractionation (an upper limit of crystallization, as suggested by Fig. 9) and an analysis of the La Huacana granite bedrock (Luhr and Carmichael, 1985). Light gray bands indicate mixing between the Jorullo melts and the granite, suggesting a role for assimilation in the later melts.

UNCORRECTED PROOF

Please cite this article as: Johnson, E.R., et al., Magmatic volatile contents and degassing-induced crystallization at Volcán Jorullo, Mexico: Implications for melt evolution and the plumbing systems..., Earth Planet. Sci. Lett. (2008), doi:10.1016/j.epsl.2008.03.004

ARTICLE IN PRESS

increasing K_2O (0.8–1.1 wt.%). Groundmass glasses have low MgO (3.7–4.3 wt.%) and higher K_2O (1.3–1.6 wt.%), indicating that extensive crystallization occurred after melt inclusion entrapment. Importantly, the lavas show increases in K_2O and decreases in CaO with decreasing MgO that differ from many of the melt inclusions. These deviations imply differences in magmatic processes for lavas and melt inclusions, and the significance of this will be discussed in Section 5.3.

Melt inclusion incompatible trace element concentrations also generally increase from the early to late stages of the eruption (Fig. 3). While some elements show steady increases from early to late in the eruption, several elements seem to be anomalously enriched in the late melt inclusions. Similar enrichments were seen in some trace elements in the late-stage lavas (Luhr and Carmichael, 1985).

The bulk tephra analyses from the early, middle and late tephra layers are all less evolved than the earliest lavas (Fig. 2), suggesting that the preserved tephra sequence that we sampled may have been erupted prior to most, if not all, of the lava flows. This interpretation is supported by descriptions of the eruption that suggest that the early phases of activity were mainly explosive and that lava flows may not have issued from the cone until the eruption was in its fifth year (Gadow, 1930). An alternative possibility is that the proximal tephra deposits that we sampled were enriched in dense olivine relative to the lower density, vesicular pyroclasts ejected during eruption and fallout of the tephra.

4.2. Olivine compositions and zoning

Comparison of olivine compositions in the tephra and lava supports our interpretation that the explosive eruptions largely preceded effusive activity, and shows that the olivine forsterite content decreased throughout the eruption. Fig. 4 shows probability density curves for olivine core compositions from the lava flows (Luhr and Carmichael, 1985) and the tephra throughout the eruption. Olivine from the early and middle tephra are overall more forsterite-rich than olivine from the early and middle lava flows, suggested they were erupted prior to effusion of the lavas. The olivine cores exhibit an increasing compositional range from the early tephra (Fo_{88-91}) to the late tephra (Fo_{83-88}) to the latest lava flows (Fo_{73-87}).

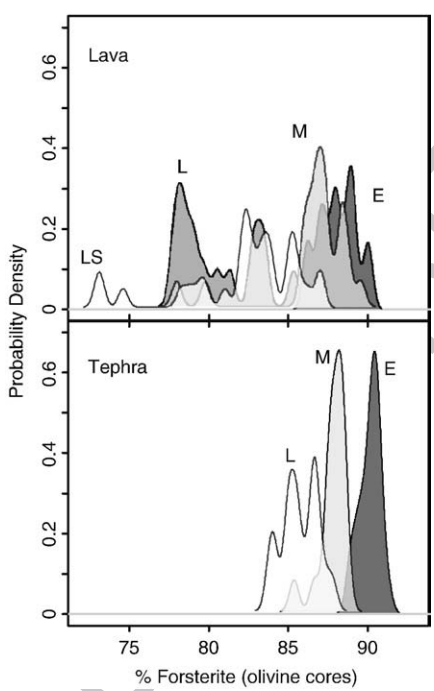

Fig. 4. Probability density curves for olivine core compositions from tephra (lower) and lava (upper; Luhr and Carmichael, 1985), where E = Early, M = Middle, L = Late (for olivine from both tephra and lava), and LS = latest (lava). These plots illustrate the general decrease in olivine core Fo-content throughout the eruption. Early and middle tephra samples appear to correspond to an earlier phase of the eruption based on high olivine Fo-content and the narrow range of olivine compositions, and the primitive composition of bulk tephra. Observations of the eruption that describe explosive activity only during the first few years of the eruption (Gadow, 1930) and a thinning of tephra onto the earliest lava flows support this interpretation. The early phase of erupted lava appears to correlate roughly with our middle to late tephra.

Olivine crystals from both the tephra and lava flows are normally zoned (Fig. 5). Zoned rims range from abrupt in the early tephra (Fig. 5a) to more gradual in the late tephra (Fig. 5b), suggesting that crystals may have resided in more evolved magmas for varying lengths of time. Using transects across these zoned crystals and the equations described earlier, we have modeled the zoning profiles (solid lines, Figs. 5a, b) and the corresponding residence times for olivine from the early, middle and late stages of the eruption. We calculate a range of olivine residence times, from ~10–200 days for the early-erupted olivine to ~80–1300 days for the late-erupted olivine (Fig. 5c). Implications for these residence times are discussed in Section 5.5.

4.3. Melt inclusion volatile concentrations

Melt inclusions preserved in Jorullo olivine trap some of the highest volatile contents yet recorded in primitive arc magmas and suggest a complex and evolving degassing history throughout the eruption (Fig. 6). Inclusions in early erupted olivine record a wide range of volatile contents and trapped both relatively undegassed melts, with up to 5.3 wt.% H_2O and 1000 ppm CO_2, and degassed melts, with low H_2O and CO_2 below detection (<50 ppm). This diversity in H_2O and CO_2 concentrations indicates that olivine crystallized over a wide range of depths, corresponding to entrapment pressures of 10 to ~400 MPa. The later-erupted inclusions are much more uniform in volatile concentrations, with all melt inclusions recording CO_2 below detection and consistently low H_2O (0.2–1.4 wt.% in middle samples; 0.4–1.0 wt.% in late samples) that indicate olivine crystallization only at very low pressures (<20 MPa). In contrast, melt inclusion S and Cl contents do not vary significantly during the eruption (S mostly 1200–1800 ppm; Cl 1000–1400 ppm, Table 1) and do not correlate with H_2O.

4.4. Groundmass crystallinity

The tephra groundmass contains abundant microlites of plagioclase, as well as minor olivine and clinopyroxene (Fig. 7a, b). Measurements of microlite abundance in the groundmass from the three tephra layers show a slight increase in crystallinity from early (41%±1%, average±1 s.e.) to late (47%±2%) in the eruption (Fig. 7c). Additionally, there are notable increases in microlite size (area), as seen visually in the comparison of the early groundmass (Fig. 7a) and late groundmass (Fig. 7b). The average size of olivine and clinopyroxene crystals increases from 60±13 μm^2 (early) to 145±13 μm^2 (late), and the average size of plagioclase laths increases from 124±7 μm^2 (early) to 180±20 μm^2 (late) (Fig. 7d).

5. Discussion

5.1. Degassing processes

The scatter in the melt inclusion H_2O and CO_2 concentrations shown in Fig. 6 reflects a complex magma degassing history. Calculated degassing paths (solid lines, Fig. 6) show that some of the variation in H_2O and CO_2 can be explained by either open-system degassing, where CO_2 degasses almost entirely with little loss of H_2O, or closed-system degassing, in which the ascending melt and exsolving gas remain in equilibrium. However, many inclusions have elevated CO_2 for a given H_2O content that cannot be explained by closed-system degassing models. Similar scatter has been seen in other magmatic systems (e.g., Rust et al., 2004; Atlas et al., 2006;

Please cite this article as: Johnson, E.R., et al., Magmatic volatile contents and degassing-induced crystallization at Volcán Jorullo, Mexico: Implications for melt evolution and the plumbing systems..., Earth Planet. Sci. Lett. (2008), doi:10.1016/j.epsl.2008.03.004

ARTICLE IN PRESS

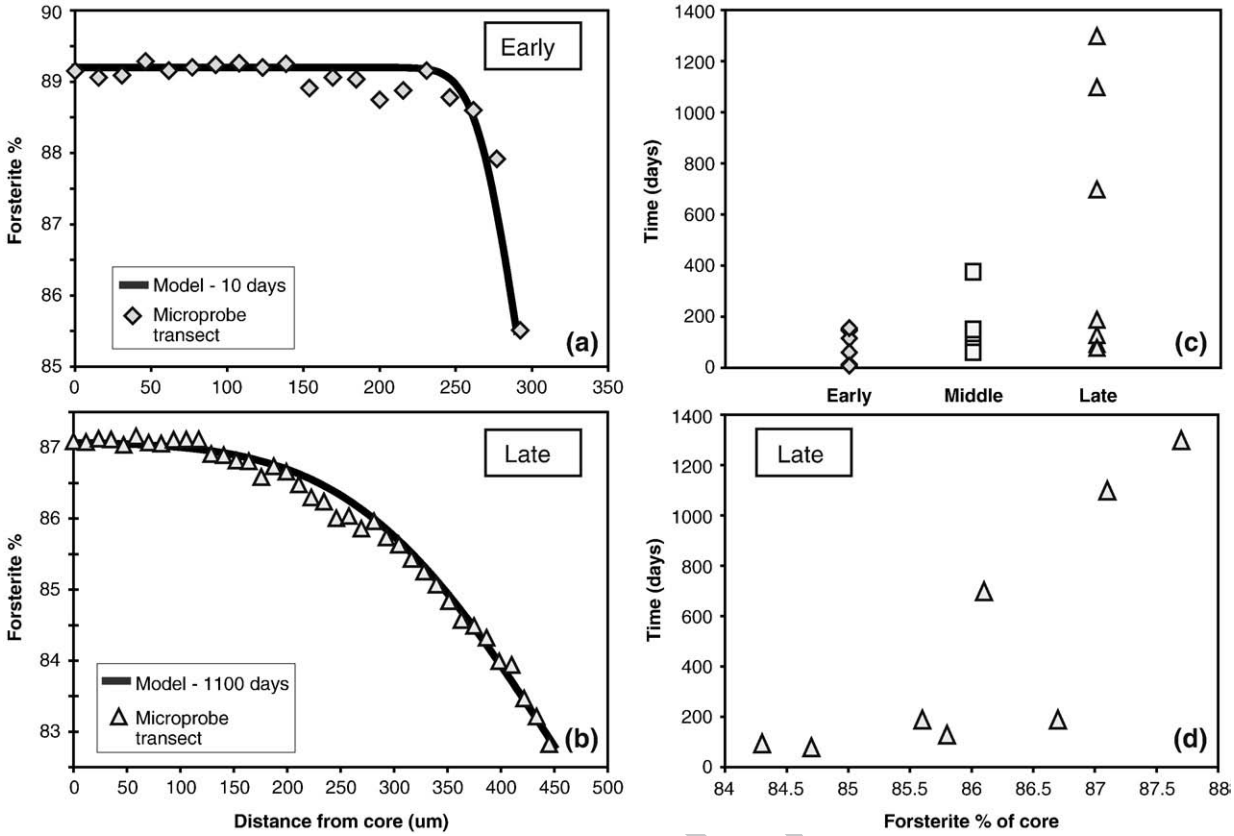

Fig. 5. Olivine zoning and residence time calculations. Fig. 5a and b show representative electron microprobe transects from core-to-rim for early and late olivine crystals, respectively. Also shown are modeled diffusion profiles (thick solid lines). Fig. 5c shows the calculated residence times for olivine from the early, middle and late stages of the tephra section. Fig. 5d illustrates the positive relationship between olivine residence time and olivine core composition from the late olivine samples. This suggests that earlier, less evolved melts crystallized olivine that then resided for potentially long periods of time in more evolved melts. Standard deviations were calculated based on multiple transects and models, but error bars are smaller than the symbol size.

Spilliaert et al., 2006). The low H_2O, high CO_2 inclusions could result from several processes, including disequilibrium degassing of melts before entrapment (Gonnermann and Manga, 2005) or post-entrapment diffusive loss of H_2 of H_2O through the melt inclusion host crystals. The former process is difficult to evaluate because of the lack of data on H_2O and CO_2 diffusivities in hydrous basaltic melts (Baker

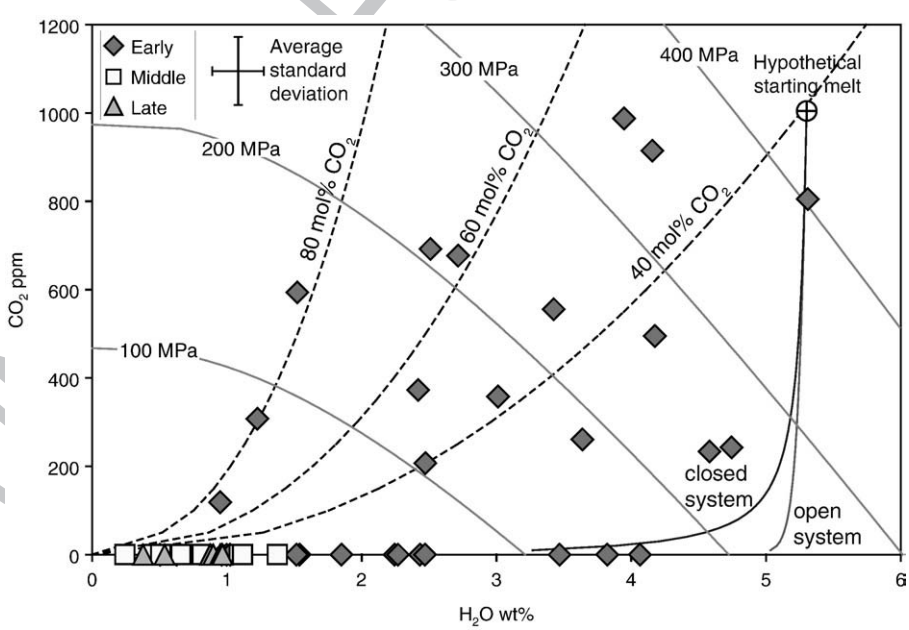

Fig. 6. Melt inclusion CO_2 vs. H_2O for early (diamonds), middle (squares), and late (triangles) samples. Also shown are calculated vapor saturation isobars, open and closed-system degassing paths, and vapor isopleths for 40, 60 and 80% CO_2, all calculated using VolatileCalc (Newman and Lowenstern, 2002). For many inclusions, the pressures based on dissolved H_2O and CO_2 are minimum values because the inclusions contain a small shrinkage vapor bubble (formed post-entrapment) that contains some additional CO_2. However, most low H_2O, low CO_2 inclusions contain no such shrinkage bubble. The average standard deviation was calculated based on multiple analyses per inclusion.

Please cite this article as: Johnson, E.R., et al., Magmatic volatile contents and degassing-induced crystallization at Volcán Jorullo, Mexico: Implications for melt evolution and the plumbing systems..., Earth Planet. Sci. Lett. (2008), doi:10.1016/j.epsl.2008.03.004

ARTICLE IN PRESS

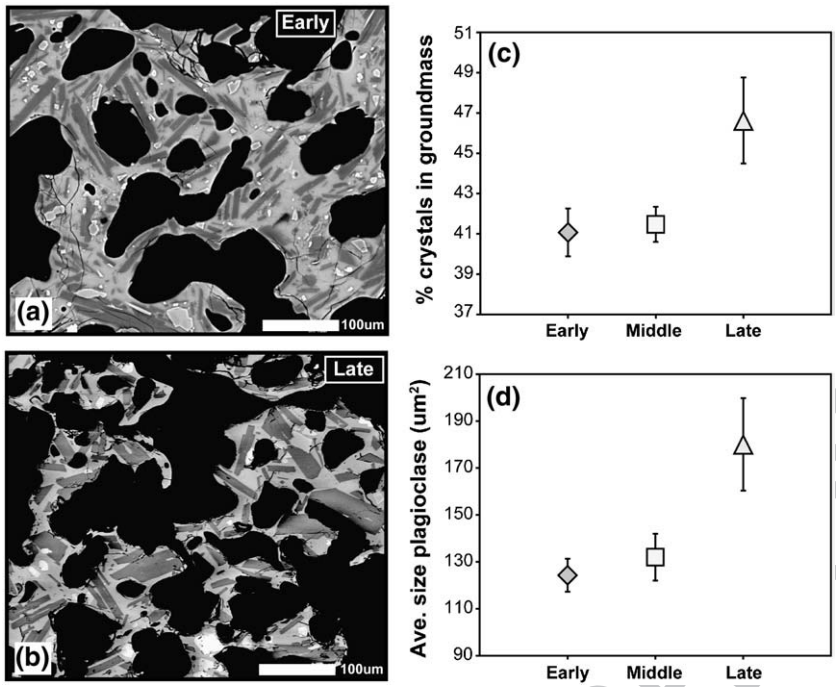

Fig. 7. Groundmass crystallinity from SEM image analyses. a and b show images of groundmass tephra from the early and late tephra samples, respectively. c shows the average crystallinity for early, middle and late samples based on SCION image analysis estimates. d shows an increase in size of groundmass plagioclase from early to late in the eruption, where size is the area of a groundmass crystal as calculated using SCION image analysis software. Error bars show ±1 standard error based on analysis of multiple images for each sample.

et al., 2005), but it is probably more effective in low temperature, silicic magmas. Loss of water by H_2 diffusion is probably limited to ≤1 wt.% H_2O by redox effects (Danyushevsky et al., 2002), and thus could not explain all of the scatter we see in our data. Loss of water by molecular H_2O diffusion through the olivine host (Portnyagin and Almeev, 2007) is not limited by redox reactions. However, the loss of 2.5 to 4 wt.% H_2O that would be required to account for our data (assuming all high CO_2 inclusions started along the closed-system degassing curve in Fig. 6) would cause considerable crystallization of olivine, plagioclase, and clinopyroxene inside the inclusions and formation of a substantial shrinkage vapor bubble. None of these features are observed in the high CO_2, low H_2O inclusions, leading us to conclude that significant H_2O diffusive loss through the host olivine has not occurred. Additionally, we see no correlation between diffusive Fe-loss from the melt inclusions (see Supplementary material) and the deviation of H_2O contents from the closed-system degassing curve in Fig. 6.

An alternative possibility is that the scatter in Fig. 6 may be the result of melts equilibrating with more CO_2-rich vapor percolating through the system from below, where it is released by magma degassing deeper in the system (Rust et al., 2004; Spilliaert, 2006). Vapors with 40–80 mol% CO_2 fit most of the scatter in our data (CO_2 vapor isopleths, dashed lines, Fig. 6). This gas fluxing hypothesis requires that melts have initially high CO_2 contents (≥0.7 wt.%) in order to create such CO_2-rich gases during ascent in the deep crust. Although such high values have not been found in melt inclusions, an analysis based on arc volcanic CO_2 fluxes suggests that such high values are common in mafic arc magmas (Wallace, 2005). The gas fluxing effect may be enhanced by repeated cycles of decompression and repressurization within the conduit (Rust et al., 2007).

The melt inclusions record evidence for loss of H_2O and CO_2 by degassing, but there is no indication of S and Cl degassing throughout the eruption, probably because these components have higher solubility. Lack of Cl degassing has been observed previously (e.g., Sisson and Layne, 1993), but the lack of S degassing is more peculiar and may result from relatively high oxygen fugacity and presence of S primarily as sulfate.

5.2. Crystallization during ascent and degassing

The primitive composition of the early Jorullo melts combined with initially high magmatic volatiles, gas fluxing, and degassing caused

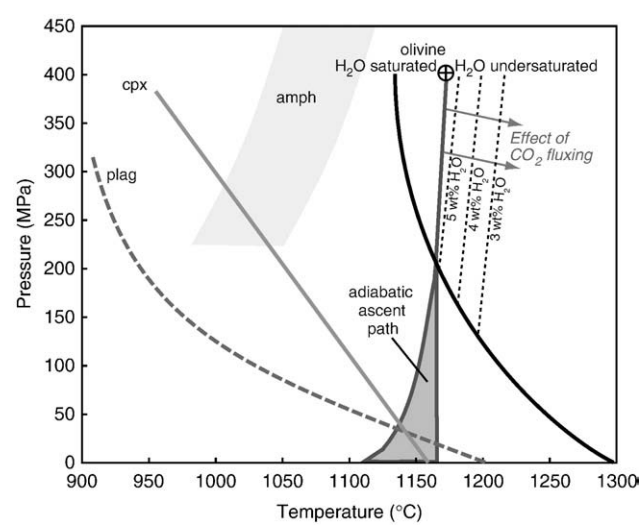

Fig. 8. Phase diagram for early Jorullo melt composition (10.5 wt.% MgO) constructed using MELTS (Ghiorso and Sack, 1995; Asimow and Ghiorso, 1998) and pMELTS (Ghiorso et al., 2002). Circle with cross indicates hypothetical starting melt based on the highest melt inclusion entrapment pressure of 400 MPa with 5.3 wt.% H_2O. The adiabatic ascent path was calculated using MELTS and pMELTS and includes the effects of crystallization, gas exsolution, and gas expansion; the widening at low pressures reflects variability between the two models. Amphibole liquidus region is based on experimental studies by Holloway (1973), Holloway and Ford (1975), Moore and Carmichael (1998), Grove et al. (2003), and Nicholis and Rutherford (2004).

UNCORRECTED PROOF

Please cite this article as: Johnson, E.R., et al., Magmatic volatile contents and degassing-induced crystallization at Volcán Jorullo, Mexico: Implications for melt evolution and the plumbing systems..., Earth Planet. Sci. Lett. (2008), doi:10.1016/j.epsl.2008.03.004

ARTICLE IN PRESS

olivine-only crystallization over the wide range of depths indicated by our melt inclusion data. These inferences are supported by a phase diagram for early Jorullo melts constructed using MELTS and pMELTS (Fig. 8). The high MgO and H_2O contents of the early Jorullo melts produce a large field of olivine-only crystallization. Melt inclusion data demonstrate that olivine crystals formed at a maximum pressure of 400 MPa; however, at this pressure the melts are H_2O-undersaturated. Deep crystallization would have been facilitated by CO_2-rich vapor fluxing through the system, as suggested by some of the melt inclusion data (Fig. 6). Fluxing of CO_2-rich gas would remove H_2O from the melt, even though the melts were H_2O undersaturated. Thus the melts would have been below their relevant H_2O undersaturated liquidii (Fig. 8), forcing small quantities of olivine to crystallize during ascent. Larger amounts of olivine would have crystallized once the melts crossed the H_2O saturated liquidus (at ~150–200 MPa).

The phase relations (Fig. 8) are also consistent with the complicated degassing history shown in the plot of CO_2 vs. H_2O (Fig. 6). In this plot there are essentially two groups of inclusions; the first group are those that roughly fit either open or closed-system degassing paths, in other words, melts that have degassed all of their CO_2 prior to olivine crystallization. These crystals would have grown along or below the H_2O-saturated olivine-in curve at pressures commencing at ~150 MPa, as recorded by the entrapment pressure of the CO_2-poor melt inclusion with the highest H_2O (Fig. 6). The second group of inclusions are those that cannot be explained by either closed or open system degassing, and instead require fluxing of CO_2-rich vapor through the system. According to our melt inclusion data, nearly all inclusions trapped at pressures >200 MPa require interaction with CO_2-rich vapor; these pressures correspond to the region above the H_2O-saturated olivine-in curve where the ability to crystallize olivine depends on addition of CO_2 and subsequent loss of H_2O from the melt.

The adiabatic ascent path in Fig. 8 shows that olivine would be the only crystallizing phase over a large range of pressures (~400–30 MPa), with plagioclase joining olivine-only at low pressures (<30 MPa), followed by near-surface crystallization of clinopyroxene. This predicted ascent and crystallization path agrees with the melt inclusion data, the modal abundance of olivine in the tephra, and the presence of late-stage plagioclase and minor clinopyroxene as groundmass crystals in the quenched tephra glass (Fig. 7a, b).

The later-erupted melt inclusions indicate that crystallization moved to shallow levels as the eruption progressed. The lower MgO content of the later melts would have decreased the olivine-only field, such that olivine could only have crystallized at pressures ≤100 MPa (based on an eruption temperature of ~1150 °C and the phase diagram of Moore and Carmichael, 1998). However, melt inclusion entrapment pressures later in the eruption vary only from 3 to 19 MPa, suggesting that either deeper crystallizing olivine fractionated out of the melt and was not erupted, or, that olivine preferentially crystallized only shallowly in the plumbing system. This shallow crystallization further suggests that the CO_2 fluxing that enabled deep olivine crystallization early had shut off later in the eruption. Additionally, some later-erupted melt inclusions show the compositional effects of plagioclase +/− clinopyroxene crystallization (see Section 5.3). These phases would also have crystallized at low pressures (<40 MPa), lending further support to the development of a shallow region of melt crystallization.

Our data show that the crystallization recorded by melt inclusions is driven by H_2O loss during ascent. At higher pressures (200–400 MPa) loss of H_2O is likely caused by gas fluxing, but at lower pressures, CO_2-depleted melts lose H_2O by direct exsolution of H_2O-rich vapor. Both processes cause melts to degas H_2O and thus can result in crystallization. Variations in K_2O, which is incompatible during crystallization, are consistent with a model of degassing-induced crystallization (Fig. 9). Based on the K_2O content of the highest pressure inclusion (0.66 wt.% K_2O), increases in K_2O with decreasing pressure for all early erupted melt inclusions are consistent with up to 14% crystallization. Later in the eruption, low pressure degassing resulted in extensive shallow crystallization of olivine,

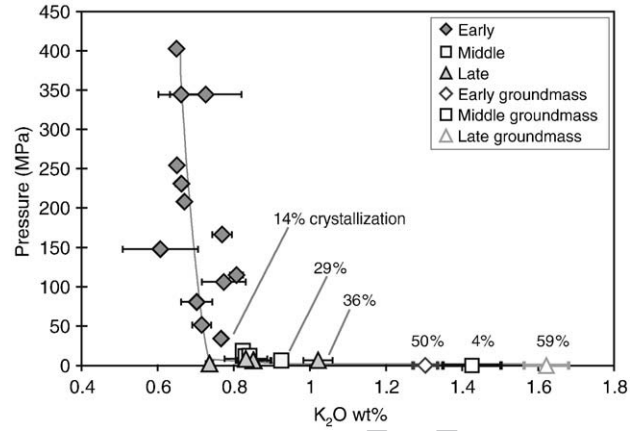

Fig. 9. Pressure (MPa) vs. K_2O for melt inclusions and groundmass glasses. Pressures for melt inclusions were calculated based on dissolved CO_2 and H_2O (Fig. 6) using the VolatileCalc solubility model (Newman and Lowenstern, 2002). Percent total crystallization required to relate various compositions to the parental melt is calculated assuming that K_2O is perfectly incompatible. Also shown is the calculated MELTS ascent path, which predicts 48% total crystallization and correlates very well with the data (gray circle). Error bars show ±1 standard deviation based on multiple analyses. Where not shown, error is smaller than symbol size.

plagioclase, and minor clinopyroxene, producing K_2O increases that require up to 29–36% crystallization prior to melt inclusion entrapment (Fig. 9).

Whereas the late inclusions were trapped shallowly (3–19 MPa), crystallization of the groundmass in the tephra clasts occurred shallower still, likely during rise in the upper conduit and during eruption. Groundmass glass analyses for the three tephra layers indicate that significant crystallization of microlites occurred after the melt inclusions were trapped (Fig. 9). The K_2O in tephra groundmass glass increases steadily from the early (1.3 wt.%) to late (1.6 wt.%) samples, corresponding to approximately 50% total crystallization (early) and 59% total crystallization (late) of initially primitive melt. These values suggest that ~25% crystallization occurred between the last melt inclusion trapped and eruption and quenching of the pyroclasts, and that much of this extensive crystallization was shallow (<10 MPa).

Additionally, the temporal increase in both crystallinity and crystal size measured in groundmass glass images (Fig. 7c, d) suggests an increased time scale for groundmass crystallization prior to eruption. This could have been achieved by either decreasing ascent rate in the latter stages of the eruption or storage of later melts en route to the surface. Shallow storage of magma at the base of a growing cinder cone has been suggested elsewhere (Krauskopf, 1948; Cervantes and Wallace, 2003; Pioli and Cashman, 2006) to explain both lava effusion from the base of cinder cones and shallow growth of olivine crystals.

5.3. Lava vs. tephra — the role of deep crustal fractionation

The melt compositions trapped in olivine during the eruption of Volcán Jorullo record the importance of olivine crystallization throughout the eruption, with the addition of shallow plagioclase +/− clinopyroxene later in the eruption. Olivine crystallization played a key role in changing the liquid composition, as evidenced by the abundance of olivine in the tephra and lava flows and the decrease in melt inclusion MgO contents as the eruption progressed (Fig. 2). Much of the melt inclusion data can be explained by ~13 wt.% olivine fractionation (solid line in Fig. 2). However, lower CaO contents in some of the later inclusions and the groundmass glass require additional crystallization of plagioclase +/− clinopyroxene (solid and dotted lines, Fig. 2b).

Whereas the melt inclusion data record crystallization of olivine ± plagioclase ± clinopyroxene in the upper crust caused by ascent and degassing, the bulk lava compositions (gray field, Fig. 2) differ from the melt inclusions, suggesting a different fractionation history. Unlike the

UNCORRECTED PROOF

Please cite this article as: Johnson, E.R., et al., Magmatic volatile contents and degassing-induced crystallization at Volcán Jorullo, Mexico: Implications for melt evolution and the plumbing systems..., Earth Planet. Sci. Lett. (2008), doi:10.1016/j.epsl.2008.03.004

ARTICLE IN PRESS

melt inclusions, the lavas gradually increase in K_2O and decrease in CaO with decreasing MgO beginning early in the eruption. As no combination of the main erupted phenocrysts (olivine ± plagioclase) can generate this trend, Luhr and Carmichael (1985) explained this evolution by high pressure fractionation of clinopyroxene, olivine, and plagioclase. However, they noted that this explanation was problematic because of the absence of clinopyroxene phenocrysts in most lavas, and abundances of a number of incompatible trace elements were not satisfactorily accounted for with this fractionation model.

The presence of amphibole phenocrysts in some of the late-stage, most evolved, Jorullo lavas (Luhr and Carmichael, 1985) provides strong evidence that at least some portion of the crystallization process occurred at pressures high enough to stabilize amphibole (>500 MPa); we propose that fractionation of amphibole + olivine ± clinopyroxene drove the bulk melt evolution at depth. We modeled simple amphibole ± olivine fractionation with major element least squares modeling using the early and late bulk lava data, the amphibole composition from an analyzed phenocryst in a late lava (Luhr and Carmichael, 1985), and Fo_{90} olivine. We found that fractionation of amphibole + olivine has a good fit ($\sum r^2 = 0.99$) compared to amphibole only ($\sum r^2 = 4.66$). Plotted in the major element diagrams of Fig. 2 is the amphibole + olivine fractionation trend (thick dashed line), which corresponds to fractionation of 17.3 wt.% amphibole and 6.7 wt.% olivine. Because there is uncertainty as to whether amphibole would have been stable in the highest temperature melts (e.g., Moore and Carmichael, 1998; Grove et al., 2003; Nicholis and Rutherford, 2004), the earliest stages of fractionation may have involved olivine + clinopyroxene, with amphibole joining the assemblage (or replacing clinopyroxene by reaction relation) at temperatures between 1100–1150 °C. We hypothesize that most of the original fractionating crystals were left behind at depth, perhaps in a deep crustal hot zone sill (Annen et al., 2006), and that ascending batches of melt then crystallized olivine during degassing. Thus most or all of the crystals in the tephra and lavas were formed during ascent, whereas the bulk composition of melt batches emanating from the deep reservoir became progressively more evolved over time due to deep fractionation.

5.4. Role of shallow assimilation — trace elements

While it seems that most of the bulk melt evolution can be explained by fractionation of amphibole + olivine ± clinopyroxene at depth, there is also evidence for shallow assimilation of granitic bedrock (Rubin et al., 2004). Granitic xenoliths were erupted in several of the middle and late lava flows at Jorullo, and in some localities are quite abundant. Disaggregated xenoliths in the lavas and the presence of plagioclase and quartz xenocrysts in thin section suggest efficient consumption of the granites by the Jorullo magmas. Additionally, some trace elements are far more enriched in the late melt inclusions and bulk lavas (Luhr and Carmichael, 1985) than would be expected from simple fractionation. Fig. 3 shows trace element data for melt inclusions and bulk tephra. The early and middle samples show increases in trace elements (Ba, La, Zr, Y) that fit well with simple fractionation (solid line). However, the late melt inclusions and late bulk tephra show enrichments in some elements (La, Zr, Y) that do not fit with the modeled 40% crystal fractionation. Also plotted in these figures are analyses of the La Huacana granite that comprises the bedrock around Jorullo and the xenoliths present in the lava flows; mixing between this granite and Jorullo melts can explain the enrichments in the later samples. Furthermore, these data suggest that the plumbing system at Jorullo evolved such that efficient assimilation of the shallow granite occurred, lending additional support to the development of a shallow storage region late in the eruption.

5.5. Olivine residence times

Olivine crystals in both the tephra and lava flows (Luhr and Carmichael, 1985) show Fo-rich cores with more evolved rims. Most olivine from the early and middle tephra have broad homogeneous cores and narrow, normally zoned rims. Olivine from the late tephra have more gradual normal zoning. We interpret the narrowness of the zoned rims in early and middle tephra to be the result of magma mixing or entrainment of earlier formed crystals by less Mg-rich melts just before eruption. Additionally, early olivine crystallized at a wide range of depths but were deposited within the same tephra layer, or eruptive unit. This suggests that olivine from various levels of the plumbing system were re-entrained by the evolving melts rising from depth, consistent with the Jorullo bulk melt evolution driven by amphibole + olivine fractionation in the middle to lower crust.

The olivine residence time data (Fig. 5c, d) also support the formation of a shallow reservoir or storage system as the eruption progressed. The range of timescales for olivine storage increases from early to late in the eruption, suggesting that longer storage of crystals is facilitated late in the eruption by such a reservoir. Additionally, the observed correlation in the late-erupted olivine between crystal residence time and olivine core compositions (Fig. 5d) suggests that the olivine with more Fo-rich cores crystallized far earlier in the eruption (with residence times up to 1300 days), and then resided at shallow levels (based on the low entrapment pressures of middle and late melt inclusions) in a more evolved melt. Together, these data require the development of a region for long-term (months to years) crystal and melt storage at shallow levels, and support the idea of deep melt evolution followed by shallow olivine-dominated crystallization.

6. Cinder cone plumbing systems

This research gives new insight into the volatile content, crystallization processes, and plumbing system evolution of a cinder cone volcano. The eruption of Jorullo is the longest historically recorded cinder cone eruption, during which time the melts evolved. By comparing the bulk lava record (Luhr and Carmichael, 1985) to the melt inclusion record, we have found evidence for a multi-stage crystallization history at Jorullo. The melt inclusions record extensive crystallization in the upper crust driven by ascent, degassing, and gas streaming, whereas the bulk lava and tephra compositions record deeper fractionation processes. Primitive, volatile-rich magma likely rose from the mantle beneath Jorullo, stalled and cooled in the lower crust, where it fractionated amphibole + olivine during the 15-yr eruption. Such "cryptic amphibole fractionation" in the lower arc crust has recently been suggested by Davidson et al. (2007) to be a widespread phenomenon.

Whereas this initial stage of fractionation was likely driven by deep cooling, the Jorullo melt inclusions record evidence for crystallization driven by degassing during magma ascent. The early Jorullo melts rose from depth, likely in a complex network of dikes and sills, and crystallized olivine from 16 km to the near-surface (calculated assuming upper crustal density of 2600 kg/m^3). Olivine crystallized at pressures of 200–400 MPa due to fluxing of CO_2-rich gases through the conduit system, which forced melts to degas H_2O, and thus placed the melts below the relevant H_2O-undersaturated olivine-in curves. Subsequent degassing under near H_2O-saturated conditions as the melts rose induced further crystallization. The later-erupted melt inclusions record a significant change in the plumbing system, with olivine crystallization localized very shallowly beneath the volcano (80–700 m) and the addition of plagioclase ± clinopyroxene as crystallizing phases.

The shallowing of olivine crystallization depths, combined with both the extensive crystallization recorded by the groundmass and the increasing olivine residence times indicated by diffusion profiles, suggest that a shallow reservoir developed as the eruption of Jorullo progressed, facilitating degassing, crystallization, and melt storage. A similar shallow degassing region was suggested by Krauskopf (1948) to explain the extrusion of degassed lava laterally from the base of Parícutin. This model would also hold for Jorullo, as degassed lavas effused from the base of the cone for much of the eruption. Additionally,

UNCORRECTED PROOF

Please cite this article as: Johnson, E.R., et al., Magmatic volatile contents and degassing-induced crystallization at Volcán Jorullo, Mexico: Implications for melt evolution and the plumbing systems..., Earth Planet. Sci. Lett. (2008), doi:10.1016/j.epsl.2008.03.004

ARTICLE IN PRESS

degassing, crystallization, and release of latent heat in this shallow network would have enabled crustal assimilation of the granitic bedrock, a process seen both at Parícutin (McBirney et al., 1987) and Jorullo (Rubin et al., 2004). Development of such a reservoir seems applicable to long-lived cinder cones like Jorullo. For example, the eruption of Parícutin lasted for nine years and the melts similarly evolved over time, both due to fractionation and assimilation (Wilcox, 1954; McBirney et al., 1987). Because such reservoirs are capable of storing melts for extended periods of time and may feed the extensive lava flows, they may be a common feature of other long-lived cinder cone eruptions.

Acknowledgements

We would like to thank Laura Pioli, Nathalie Vigouroux, Elizabeth Erlund and Colleen Donegan for help during field work, and Tom Sisson and Greg Valentine for thorough reviews that greatly improved the final manuscript. This research was supported by NSF grants EAR-0309559 and EAR-0510493.

Appendix A. Supplementary data

Supplementary data associated with this article can be found, in the online version, at doi:10.1016/j.epsl.2008.03.004.

References

Annen, C., Blundy, J.D., Sparks, R.S.J., 2006. The genesis of intermediate and silicic magmas in deep crustal hot zones. J. Petrol. 47 (3), 505–539.
Asimow, P.D., Ghiorso, M.S., 1998. Algorithmic modifications extending MELTS to calculate subsolidus phase relations. Am. Mineral. 83, 1127–1131.
Atlas, Z.D., Dixon, J.E., Sen, G., Finny, M., Martin-Del Pozzo, A.L., 2006. Melt inclusions from Volcán Popocatépetl and Volcán de Colima, Mexico: melt evolution due to vapor-saturated crystallization during ascent. J. Volcanol. Geotherm. Res. 153, 221–240.
Baker, D.R., Freda, C., Brooker, R.A., Scarlato, P., 2005. Volatile diffusion in silicate melts and its effects on melt inclusions. Ann. Geophys. 48 (4/5), 699–717.
Blundy, J., Cashman, K., Humphreys, M., 2006. Magma heating by decompression-driven crystallization beneath andesite volcanoes. Nature 443, 76–80.
Cervantes, P., Wallace, P.J., 2003. Role of H_2O in subduction-zone magmatism: new insights from melt inclusions in high-Mg basalts from central Mexico. Geology 31, 235–238.
Costa, F., Chakraborty, S., 2004. Decadal time gaps between mafic intrusion and silicic eruption obtained from chemical zoning patterns in olivine. Earth Planet. Sci. Lett. 227, 517–530.
Davidson, J., Turner, S., Handley, H., Macpherson, C., Dosseto, A., 2007. Amphibole "sponge" in arc crust? Geology 35 (9), 787–790.
Danyushevsky, L.V., Sokolov, S., Falloon, T.J., 2002. Melt inclusions in olivine phenocrysts: using diffusive re-equilibration to determine the cooling history of a crystal, with implications for the origin of olivine-phyric volcanic rocks. J. Petrol. 43, 1651–1671.
Dixon, J.E., Pan, V., 1995. Determination of the molar absorptivity of dissolved carbonate in basanitic glass. Am. Mineral. 80 (11–12), 1339–1342.
Dixon, J.E., Stolper, E.M., Holloway, J.R., 1995. An experimental study of water and carbon dioxide solubilities in mid-ocean ridge basaltic liquids. Part I: calibration and solubility models. J. Petrol. 36 (6), 1607–1631.
Dohmen, R., Chakraborty, S., Palme, H., Rammensee, W., 2003. Role of element solubility on the kinetics of element partitioning: in situ observations and a thermodynamic kinetic model. J. Geophys. Res. 108 (B3), 2157. doi:10.1029/2002JB000587.
Gadow, H., 1930. Jorullo: The History of the Volcano of Jorullo and the Reclamation of the Devastated District by Animals and Plants. Cambridge Univ. Press, London, p. 101.
Ghiorso, M.S., Sack, R.O., 1995. Chemical mass transfer in magmatic processes. IV. A revised and internally consistent thermodynamic model for the interpolation and extrapolation of liquid–solid equilibria in magmatic systems at elevated temperatures and pressures. Contrib. Mineral. Petrol. 119, 197–212.
Ghiorso, M.S., Hirschmann, M.M., Reiners, P.W., Kress III, V.C., 2002. The pMELTS: a revision of MELTS aimed at improving calculation of phase relations and major element partitioning involved in partial melting of the mantle at pressures up to 3 GPa. Geochem. Geophys. Geosyst. 3 (5). doi:10.1029/2001GC000217.
Gonnermann, H.M., Manga, M., 2005. Nonequilibrium magma degassing: results from modeling of the ca. 1340 AD eruption of Mono Craters, California. Earth Planet. Sci. Lett. 238, 1–16.
Grove, T.L., Elkins-Tanton, L.T., Parman, S.W., Chatterjee, N., Müntener, O., Gaetani, G.A., 2003. Fractional crystallization and mantle-melting controls on calc-alkaline differentiation trends. Contrib. Mineral. Petrol. 145, 515–533.
Hasenaka, T., Carmichael, I.S.E., 1985. The cinder cones of Michoacán–Guanajuato, central Mexico: their age, volume and distribution, and magma discharge rate. J. Volcanol. Geotherm. Res. 25, 105–124.
Hildreth, W., Moorbath, S., 1988. Crustal contributions to arc magmatism in the Andes of central Chile. Contrib. Mineral. Petrol. 98, 455–489.
Holloway, J.R., 1973. The system pargasite–H_2O–CO_2: a model for melting of a hydrous mineral with a mixed-volatile fluid — I. Experimental results to 8 kbar. Geochim. Cosmochim. Acta 37, 651–666.
Holloway, J.R., Ford, C.E., 1975. Fluid absent melting of the fluorohydroxy-amphibole pargasite to 35 kilobars. Earth Planet. Sci. Lett. 25, 44–48.
Jurewicz, A.J.G., Watson, E.B., 1988. Cations in olivine: Part 2. Diffusion in olivine xenocrysts, with applications to petrology and mineral physics. Contrib. Mineral. Petrol. 99, 186–201.
Kent, A.J.R., Stolper, E.M., Francis, D., Woodhead, J., Frei, R., Eiler, J., 2004. Mantle heterogeneity during the formation of the North Atlantic Tertiary Province: constraints from trace element and Sr–Nd–Os–O isotope systematics of Baffin Island picrites. Geochem., Geophys., Geosyst. (5), Q11004. doi:10.1029/2004GC000743.
Krauskopf, K., 1948. Mechanism of eruption at Parícutin volcano, México. Geol. Soc. Amer. Bull. 59, 711–731.
Luhr, J.F., 2001. Glass inclusions and melt volatile contents at Parícutin Volcano, Mexico. Contrib. Mineral. Petrol. 142, 261–283.
Luhr, J.F., Carmichael, I.S.E., 1985. Jorullo Volcano, Michoacán, Mexico (1759–1774): the earliest stages of fractionation in calc-alkaline magmas. Contrib. Mineral. Petrol. 90, 142–161.
McBirney, A.R., Taylor Jr., H.P., Armstrong, R.L., 1987. Parícutin re-examined: a classic example of crustal assimilation in calc-alkaline magma. Contrib. Mineral. Petrol. 95, 4–20.
Métrich, N., Bertagnini, A., Landi, P., Rosi, M., 2001. Crystallization driven by decompression and water loss at Stromboli Volcano (Aeolian Islands, Italy). J. Petrol. 42, 1471–1490.
Moore, G., Carmichael, I.S.E., 1998. The hydrous phase equilibria (to 3 kbar) of and andesite and basaltic andesite from western Mexico: constraints on water content and conditions of phenocrysts growth. Contrib. Mineral. Petrol. 130, 304–319.
Newman, S., Lowenstern, J.B., 2002. VolatileCalc: a silicate melt–H_2O–CO_2 solution model written in VISUAL BASIC Excel. Comput. Geosci. 28, 597–604.
Nicholis, M.G., Rutherford, M.J., 2004. Experimental constraints on magma ascent rate for the crater flat volcanic zone hawaiite. Geology 32 (6), 489–492.
Pardo, M., Suárez, G., 1995. Shape of the subducted Rivera and Cocos plates in southern Mexico: seismic and tectonic implications. J. Geophys. Res. 100 (B7), 12357–12373.
Pioli, L., Cashman, K.V., 2006. Application of two-phase flow models along vertical pipes for the description of basaltic explosive volcanic activity. Eos Trans. AGU 87 (52) Fall Meet. Suppl., Abstract V43C-1812.
Portnyagin, M., Almeev, R., 2007. Experimental evidence for rapid re-equilibration of water between melt inclusions in olivine and host magma. Geochim. Cosmochim. Acta 71 (15), A804.
Roberge, J., Wallace, P.J., White, R.V., Coffin, M.F., 2005. Anomalous uplift and subsidence of the Ontong Java Plateau inferred from CO_2 contents of submarine basaltic glasses. Geology 33 (6), 501–504.
Roggensack, K., 2001. Sizing up crystals and their melt inclusions; a new approach to crystallization studies. Earth Planet. Sci. Lett. 187, 221–237.
Roggensack, K., Hervig, R.L., McKnight, S.B., Williams, S.N., 1997. Explosive basaltic volcanism from Cerro Negro volcano: influence of volatiles on eruptive style. Science 277, 1639–1642.
Rubin, K.H., Jurado-Chichay, Z., Pyle, D., Morán-Zenteno, D., Rowland, S., 2004. El Jorullo revisited: petrology, geochemistry & volcanology. Eos Trans. AGU 85 (47) Fall Meet. Suppl., Abstract V13B-1485.
Rust, A.C., Cashman, K.V., Wallace, P.J., 2004. Magma degassing buffered by vapor flow through brecciated conduit margins. Geology 32, 349–352.
Rust, A., Blundy, J., Cashman, K., 2007. Melt CO_2 enrichment by permeable flow and resorption. Eos Trans. AGU 88 (52) Fall Meet. Suppl., Abstract V21C-0729.
Sisson, T.W., Layne, G.D., 1993. H_2O in basalt and basaltic andesite glass inclusions from four subduction-related volcanoes. Earth Planet. Sci. Lett. 117, 619–635.
Sobelev, A.V., Chaussidon, M., 1996. H_2O concentrations in primary melts from supra-subduction zones and mid-ocean ridges; implications for H_2O storage and recycling in the mantle. Earth Planet. Sci. Lett. 137 (1–4), 45–55.
Spilliaert, N., Allard, P., Métrich, N., Sobolev, A.V., 2006. Melt inclusion record of the conditions of ascent, degassing, and extrusion of volatile-rich alkali basalt during the powerful 2002 flank eruption of Mount Etna (Italy). J. Geophys. Res. 111. doi:10.1029/2005JB003934.
Sugawara, T., 2000. Empirical relationships between temperature, pressure, and MgO content in olivine and pyroxene saturated liquid. J. Geophys. Res. 105 (B4), 8457–8472.
Valentine, G.A., Krogh, K.E.C., 2006. Emplacement of shallow dikes and sills beneath a small basaltic volcanic center — the role of pre-existing structure (Paiute Ridge, southern Nevada, USA). Earth Planet. Sci. Lett. 246, 217–230.
Vespermann, D., Schmincke, H.-U., 2002. Scoria cones and tuff rings. In: Sigurdsson, H., Houghton, B.F., McNutt, S.R., Rymer, H., Stix, J. (Eds.), Encyclopedia of Volcanoes. Academic Press, San Diego, pp. 683–694.
Wade, J.A., Plank, T., Melson, W.G., Soto, G.J., Hauri, E.H., 2006. The volatile content of magmas from Arenal volcano, Costa Rica. J. Volcanol. Geotherm. Res. 157, 94–120.
Wallace, P.J., 2005. Volatiles in subduction zone magmas; concentrations and fluxes based on melt inclusion and volcanic gas data. J. Volcanol. Geotherm. Res. 140 (1–3), 217–240.
Wilcox, R.E., 1954. Petrology of Paricutin volcano, Mexico. U.S. Geol. Surv. Bull. 281–354.
Wood, C.A., 1980. Morphometric evolution of cinder cones. J. Volcanol. Geotherm. Res. 7, 387–413.

UNCORRECTED PROOF

Please cite this article as: Johnson, E.R., et al., Magmatic volatile contents and degassing-induced crystallization at Volcán Jorullo, Mexico: Implications for melt evolution and the plumbing systems..., Earth Planet. Sci. Lett. (2008), doi:10.1016/j.epsl.2008.03.004